Probing Electrolyte Solvents at Solid/Liquid 1

Interface using Gap-Mode Surface-Enhanced Raman 2

Spectroscopy 3

- Guang Yang^{a*}, Robert L. Sacci^a, Ilia N. Ivanov^b, Rose E. Ruther^c, Kevin A. Hays^c, Yiman Zhang^a, 4
- Peng-Fei Cao^a, Gabriel M. Veith^a, Nancy J. Dudney^a, Tomonori Saito^a, Daniel T. Hallinan^{d*}, 5
- Jagjit Nanda^{a*} 6
- 7 Chemical Sciences Division, Oak Ridge National Laboratory, Oak Ridge, Tennessee a.
- 8 37831, United States
- 9 Center for Nanophase Materials Sciences, Oak Ridge National Laboratory, Oak Ridge, b.
- 10 Tennessee 37831, United States
- 11 c. Oak Ridge National Laboratory, Energy and Transportation Science Division, Oak
- Ridge, TN 37831, USA 12

17

- 13 d. Department of Chemical and Biomedical Engineering, Florida A&M University-Florida
- 14 State University College of Engineering, Tallahassee, FL 32310, USA
- 15 KEYWORDS electrolyte structure, electrode/electrolyte interface, gold nanoparticle, surface
- 16 enhanced Raman spectroscopy, fluoroethylene carbonate, ethylene carbonate, diethyl carbonate

This manuscript has been authored by UT-Battelle, LLC under Contract No. DE-AC05-00OR22725 with the U.S. Department of

¹⁸ 19 20 21 22 23 Energy. The United States Government retains and the publisher, by accepting the article for publication, acknowledges that the

United States Government retains a non-exclusive, paid-up, irrevocable, worldwide license to publish or reproduce the published form of this manuscript, or allow others to do so, for United States Government purposes. The Department of Energy will

provide public access to these results of federally sponsored research in accordance with the DOE Public Access Plan

⁽http://energy.gov/downloads/doe-public-access-plan).

24 ABSTRACT

25

26

27

28

29

30

31

32

33

34

35

36

37

38

39

40

41

42

43

44

45

46

Understanding the aprotic solution structures at the immediate vicinity of solid/liquid interface (SLI) is critically important for next generation lithium ion battery development. Yet, it is still challenging to investigate the carbonate chemical profiles close to the diffuse layer (about 10 nm) of the electrical double layer at SLI due to the lack of a ultrahigh surface sensitive tool. In this work, we demonstrate the structures of commonly used carbonate solvents (ethylene carbonate (EC) and diethyl carbonate (DEC)) and an carbonate additive (fluoroethylene carbonate (FEC)) in a commercial Li-ion battery electrolyte can be determined at ~17 nm above the electrode surface. This is only enabled by a nanogap surface-enhanced Raman spectroscopy (SERS) technique based on a monolayer gold nanoparticle (Au NP) ensemble. The SERS enhancement factor (EF) of those carbonates was found to depend on the molecular polarizability, with the maximum EF at $\sim 10^5$ found for EC and FEC. Despite of their alike chemical structures, this monolayer Au NP SERS substrate is fully capable of discrimiating the different Raman finger prints of EC and FEC. Compared to EC, several vibration modes in FEC, such as C-C skeletal deformation, ring breathing band and C=O stretching band, shift to higher frequencies because of the displacement of a hydrogen atom by a much heavier fluorine atom in a methylene bridge. This counterintuitive observation against the commonly used "ball and spring" model in vibrational spectroscopy is mostly due to the increased bond strength in the FEC ring versus that of EC. A second order empirical polynomial of a single indeterminate best describes the correlation between the SERS band integration of EC or DEC molar concentration. Our findings open up new opportunities for in-depth understanding of the electrolyte molecular vibrational behaviors at direct solid/liquid interface and developing advanced electrolytes for next generation lithium-ion batteries.

47 Introduction

48

49

50

51

52

53

54

55

56

57

58

59

60

61

62

63

64

65

66

67

68

69

The lithium-ion battery (LIB) has dominated the consumer electronics market more than two decades since its commercialization. The increasing demand on LIB applied in the electric vehicle in recent years casts even higher requirement on its energy and power density, cyclability, safety, etc. While the significant advancement of both cathode and anode has been made, less focus has been put on the electrolyte development, resulting in an incremental LIB electrolyte improvement. (1) The electrolyte plays a crucial role in a LIB, especially with recently developed advanced anodes and cathodes. The ion exchange and redox reaction occur in the immediate vicinity of the solid electrode/liquid electrolyte interface (SLI), which is one of the major rate limiting factor in LIB. (2) In addition, due to the thermodynamic instability, the electrolyte reduction at the negative anode or oxidation at the positive cathode at SLI result in the formation of a solid electrolyte interface (SEI), which has direct impact on the Coulombic efficiency, cycle performance and safety of the LIB. (3) Thus, it is desired to unravel the molecular structures behind important processes at the SLI. Unfortunately, commonly used vibrational spectroscopic techniques (e.g. Raman and infrared spectroscopy) only allows for probing the molecular vibrations from a micron scale through the SLI, which is difficult to be distinguished from that of the bulk electrolytes far from the solid surface. (4) The LIB electrolyte is usually composed of a lithium salt (e.g. lithium hexafluorophosphate, LiPF₆) and a binary carbonate solvent (e.g. ethylene carbonate, EC, and diethyl carbonate, DEC, mixture). The nature and properties of the binary electrolyte determine the lithium salt solvation into ions and the solvated ion transport in a solvation shell. (5) The cyclic carbonates such as EC have high dielectric constant, which dissolves lithium salt better, but leads to more viscous electrolyte, leading to a lower ion mobility. On the other hand, the acyclic linear carbonate

molecules such as DEC decreases the electrolyte viscosity, assuring a high lithium ion mobility at room temperature. (6) The competitive coordination of the cyclic carbonate and the linear aprotic molecules to the Li⁺ cations complicates the interpretation of the related vibrational bands, especially distinguishing the difference on the same functional group. For example, after coordination to Li⁺, the C-O stretching mode of EC superimposes with that of DEC at around 905 cm⁻¹, preventing the clear determination of the relative intensity of component spectra at this region. (4, 7) It is thus desired to inspect the vibrational signatures of the pure carbonate solvent molecules at the SLI region. The reductive decomposition of the EC molecules on conventional graphite anode during the first charge/discharge cycle leads to SEI formation, which prevents further electrolyte decomposition. (8) However, for the high capacity silicon anode, the SEI generated from EC reduction has been found unstable, leading to poor cycling performance of silicon anodes. (9) Fluoroethylene carbonate (FEC) has proven particularly effective in protecting the silicon anode surface by creating a thinner and more homogeneous SEI than that of EC alone. (10) In addition, FEC has been found a useful additive to extend the electrochemical stability window of the carbonate electrolytes, rendering them compatible with the 5V class of cathodes such as LiN_{0.5}Mn_{1.5}O₄ and LiCoPO₄. (1, 11) Despite those promising findings, the exact redox chemistry to form a more protective SEI on the electrode surface from the FEC decomposition is still unclear and the interpretation is under debate. (12) Notably, EC and FEC have a similar molecular structure, of which vibrational modes overlap in corresponding frequency regions. Moreover, the competitive coordination of Li⁺ to EC and FEC molecules creates more complex Raman spectra, which complicates spectral studies exploring SEI formation from

70

71

72

73

74

75

76

77

78

79

80

81

82

83

84

85

86

87

88

89

90

electrolytes containing both EC and FEC. Therefore, it is imperative to develop the fundamental understanding of the molecular signatures of the pure EC and FEC on the SLI.

Using a gold nanoparticle (Au NP) nanogap-mode surface-enhanced Raman spectroscopy (SERS), we recently demonstrated that the solution structure of a commercial Li-ion battery electrolyte (1 M LiPF₆ in EC-DEC binary solvent) could be investigated at the SLI. (4) Such a nanogap mode SERS is enabled by an Au NP monolayer deposited on a solid surface, with the enhanced electromagnetic field (EM-field) concentrated between adjacent Au NPs (so called "hot spot"). The hot spot maximum was determined to be ~ 17 nm from the solid substrate surface, and the Raman intensity of the aprotic species was enhanced by about 8 orders of magnitude. (4) In this contribution, we extend the nanogap SERS platform to gain insights from the vibration signatures of three model electrolyte species – EC, DEC and FEC from the SLI region. The intense SERS signal of each species provides ease for probing the molecular fingerprints at the SLI. The distinct blueshift of several vibrational bands of FEC versus that of EC is thought to stem from stiffer bonds upon the replacement of a proton at the methylene bridge of the aprotic ring by a heavier fluorine atom. An empirical second order polynomial best describes the dependence of the integrated SERS bands on EC molar concentration in EC-DEC binary solvents, which indicates that the nanogap SERS can be used to quantify the components in the mixture solvents. Our findings here provide a protocol to explore the interfacial ion solvation, charge transport, and SEI formation and evolution in various electrochemical energy generation.

- Experimental section
- 113 Materials

92

93

94

95

96

97

98

99

100

101

102

103

104

105

106

107

108

109

110

111

114 All materials used to synthesize and self-assemble Au NPs have been reported before. (4, 13) Transparent high barrier (HB) film (ScotchpakTM HB428E) was kindly donated by 3M. Ethylene 115 116 carbonate (EC, anhydrous, > 99%), diethyl carbonate (DEC, anhydrous, > 99%) and 117 fluoroethylene carbonate (FEC, 99%) were purchased from BASF. Aluminum laminated film 118 (EQ-alf-400-7.5M) was purchased from MTI. All materials were used as received. 119 Au NP synthesis, monolayer self-assembly and transparent Raman cell fabrication 120 Au NP aqueous colloid was fabricated using a "seed-growth" method as previously reported. 121 (13) And a "three-phase" self-assembly technique was employed to assembly and deposit the Au 122 NP monolayers onto a thin film Ni-coated quartz substrate. Thin Ni film was deposited by 123 magnetron sputtering and evaporation from commercially available targets in an in-house 124 sputtering system. 5 nm Cr (99.99%, Kurt J. Lesker) was deposited as an adhesion layer, 125 followed by a Ni (99.99%, Kurt J. Lesker, 100 nm) layer. (14) The transparent Raman pouch cell 126 was fabricated in an argon-filled glovebox ($O_2 < 1$ ppm, $H_2O < 0.1$ ppm). (4) HB film and Al 127 pouch with precut sizes were sealed by an impulse heat sealer (AIE200) together with Au 128 monolayer/Ni substrate and 200 µL liquid sample sandwiched in between. 129 Characterizations 130 The micrographs of the Au NP monolayers were obtained by a scanning electron microscope 131 (SEM, Hitachi S4800, accelerating voltage = 20 kV, probe current = $20 \mu\text{A}$) and a transmission 132 electron microscopy (TEM, JEOL 2011, accelerating voltage = 200 kV, probe current = 117 133 μA). SERS experiments were performed on a Raman spectroscope (in Via Renishaw, 785 nm, 134 objective = 20 time magnification with numerical aperture (N.A.) = 0.42, local power ≤ 2 mW, 135 exposure time = 10 s, scanning number = 1). An IR spectrum of each sample was collected from

a Fourier Transform Infrared (FTIR) spectrometer (Bruker, ALPHA) with a diamond attenuated 136 total reflection (ATR) accessory (wavenumber ranges from 4000 to 650 cm⁻¹ with 128 scans). 137 138 The IR measurements were conducted in an Argon-filled glove box with O_2 and $H_2O < 0.1$ ppm. 139 The refractive indices of the EC-DEC binary solvents were measured by a refractometer (Mettler 140 Toledo, RM40) with the incident light at 589.3 nm. 141 Computational simulations 142 Finite-difference time domain (FDTD) simulation 143 A three-dimensional (3D) FDTD simulation was performed to determine the EM-field 144 distribution in the Au NP monolayer using commercially available software, Lumerical FDTD 145 Solutions. The simulation object was arrays of Au spheres with local HCP structure deposited 146 on a Ni substrate. The geometric dimensions of the Au sphere arrays were based on the results 147 of TEM measurements of the Au NP average diameter (36.7 nm) and the interparticle distance 148 (1.6 nm), (13) The numerical mesh size was set to 0.1 nm for all cases, such that there were 16 149 mesh points between even the narrowest particle gaps. 150 Density Functional Theory (DFT) calculations 151 Density functional theory (DFT) calculations implemented in GAMESS software were used to 152 optimize molecular geometries and to determine Raman scattering frequencies. (15) All DFT 153 calculations were conducted by Becke, 3-parameter, Lee-Yang-Parr (B3LYP) (16) density 154 functional algorithm with the 6-31+G(d, p) basis set.(17) The scaling factor was 1 for each 155 aprotic molecule in the present study. No symmetry restrictions were implemented to FEC, while 156 a 2-fold rotational axis (C₂) symmetry was used for EC and DEC. All molecules and the

vibrational modes were visualized with the software package "Macmolplt". (18) To obtain the predicted Raman spectra, the Lorentzian band shape with full width at half maximum (FWHM) of 10 cm⁻¹ was convoluted with the calculated Raman bands by the software GaussSum 3.0. (19)

Results and discussion

157

158

159

160

161

162

163

164

165

166

167

168

169

170

171

172

173

174

175

176

177

178

179

The local ordering of the Au NP monolayer (Au NP diameter = 36.7 nm) is confirmed by TEM and SEM micrographs. The TEM micrograph in the upper-left panel of Figure 1(a) shows that the Au NP film has a local hexagonal close packed (HCP) structure. (20) Its corresponding fast Fourier transform (FFT) features a Bragg pattern in the frequency domain that is characteristic of an HCP structure. (21) The high-magnification TEM micrograph in the lower-left panel of Figure 1(a) clearly shows that the gap between adjacent Au NPs is less than 2 nm. The average nanogap size was estimated at 1.6 nm, (4) based on analysis on at least three TEM micrographs and 500 Au NPs. Nano-sized gaps between metallic objects cause enormous increases in Raman scattering intensity. This is ascribed to the constructive interference of the localized surface plasmon (where a "hot spot" locates) on adjacent nano objects. (22) For EM-field-coupled nanoparticles, the Raman intensity, I_{SERS}, increases exponentially with decrease of interparticle spacing. (23) However, when d is too small, either the available EM field volume decreases for the analyte molecules, (24) or quantum tunneling between adjacent particles occurs, (25) thus eventually decreasing the Raman intensity. The average gap size in the current study allows for probing approximately 200 carbonate molecules on average for each nanogap. SEM image (Figure 1(a), right panel) shows a 4 µm² section of the Au NP monolayer, twice that of the Raman laser spot size. The consistency of the monolayer, particle size, and relative orientation (HCP structure) create a homogeneous SERS response. (13) FDTD simulation was used to assess the SERS enhancement factor (EF) distribution across the Au NP monolayer, as shown in Figure

1(b). The EF is a characteristic value to quantify the SERS performance of the substrate, which is estimated as the 4th power of the local enhanced EM-field normalized to that without enhancement. (13) The maximum EF ($\sim 10^8$) occurs in the nanogap region, 17 nm away from the Ni surface, demonstrating that nanogap SERS allows the spectral vibrations of the carbonate molecules used in this study to be probed in the immediate vicinity of the SLI. The well-ordered Au NP film as the gap-mode SERS substrate also allows for the precise control of the distance of the hot spot arrays from the solid surface. We do not expect smooth Ni surface contribute much to the SERS signal, as depicted from EM distribution on Ni surface without the Au NP on top in Figure 1(b). Ni coating on the surface serves as an electron conducting layer for future in operando SERS study. (4) Notably, the simulated EM distribution in different nanogaps slightly varies. This might be due to that we implemented "perfectly matched layer" boundary condition for the 3D FDTD model (details can be found in the supporting information of Reference (14)). Remarkable Raman bands are exhibited for FEC, EC, and DEC in the presence of the Au NP monolayer (Figure 2(a)), whereas no prominent peaks show up without the Au NP monolayer (i.e. standard Raman spectra with the same spectroscope settings). Readers may resort to Table S1, S2 and S3 for detailed Raman peak assignment for DEC, EC and FEC, respectively. The peak of the maximum intensity for DEC is located at 902 cm⁻¹ and is attributed to the DEC O-C-O bending band, δ_{0-c-0} . ²⁷ Vibrations related to DEC methyl groups appear between 1100 cm⁻¹ and 1500 cm⁻¹ (e.g. CH₃ rocking band occurs at 1122 cm⁻¹). Those bands do not show up in the SERS spectra of FEC and EC due to their lack of methyl groups. Compared with the SERS spectra of the linear DEC molecule, those of EC and FEC exhibit several bands related to the ring structure. For example, the maximum SERS intensity for EC is located at 897 cm⁻¹ and represents the ring skeletal deformation mode, β_{C-C} . The SERS band of the second highest

180

181

182

183

184

185

186

187

188

189

190

191

192

193

194

195

196

197

198

199

200

201

intensity was observed at 717 cm⁻¹ and is ascribed to the EC ring breathing mode, EC o_{O-C-O}. 203 204 Interestingly, the FEC ring skeletal deformation mode, FEC β_{C-C} , and the ring breathing mode, FEC o_{O-C-O}, are blueshifted with respect to EC and located at 908 cm⁻¹ and 729 cm⁻¹, 205 respectively. It is worth noting that the EC ring breathing mode occurs at 729 cm⁻¹ when 206 coordinated to Li⁺, (4) which convolutes with the FEC o_{O-C-O} band. The FEC ring skeletal 207 stretching mode (FEC v_{O-C-O}) centered at 1000 cm⁻¹ whereas the counterpart from EC (EC v_{O-C-O}) 208 is located at 975 cm⁻¹. A doublet of EC is observed at 1781 and 1807 cm⁻¹, which is attributed to 209 210 EC carbonyl stretching, $v_{C=0}$, and combination of $v_{C=0}$ with the first overtone of EC ring 211 breathing, respectively. The corresponding FEC C=O stretching doublet also exhibits a blueshift with respect to EC to 1814 and 1835 cm⁻¹, respectively. 212 213 To evaluate the SERS response of EC, DEC and FEC on Au NP monolayers, experimental EF was calculated using EF = $(I_{SERS}/I_o)^2$. I_{SERS} and I_o are the integrated SERS and corresponding 214 215 normal Raman bands, respectively. (14) Figure 2(b) exhibits the calculated EF of several Raman bands of interest for each species. The EF calculated for DEC δ_{O-C-O} bending band is 4.2 x10⁴, 216 217 one order magnitude lower than that of the EC β_{C-C} ring skeletal deformation band and the FEC 218 C-F stretching band. This is due to a higher dielectric constant of EC and FEC than that of the 219 DEC, which leads to a higher molecular polarizability. (4, 26) It is worth noting that the 220 experimental EF of these three species is 3 to 4 orders lower than the maximum values calculated by FDTD simulations, but comparable to the average FDTD EF (5.7 x 10⁵) in the gap region. 221 222 The average FDTD EF was estimated by averaging all EF across the center plane (1.6 nm × 23.4 223 nm) in the nanogap region that is parallel to the Ni surface. 224 As mentioned above, the FEC carbonyl and ring-related Raman bands blueshift with respect to 225 those for EC upon a hydrogen atom being replaced by a heavier fluorine atom in a methylene

bridge. This is shown in more detail in Figure 3. This observation contradicts the "ball and spring" model, which predicts a reduced frequency upon the replacement of a light atom by a heavier one. (26) However, DFT calculations on the Raman spectra of EC and FEC exhibit the same trend as experiment (Figure 3, lower panel), which indicates the mechanism cannot be explained by blindly using the "ball and spring" model. The "ball and spring" model assumes two atoms (A and B) are bonded by a spring, and the vibrational frequency, v, can thus be calculated by

$$233 v = \frac{1}{2\pi c} \sqrt{\frac{f}{\mu}}, (1)$$

with c being the velocity of light, f the spring constant, and μ the reduced mass of atoms A and

235 B;

243

244

245

246

236
$$\mu = \frac{M_A M_B}{M_A + M_B}.$$
 (2)

in which M_A and M_B are masses of atoms A and B. From equation 1, the frequency of a specific vibrational mode is not only determined by the reduced mass, μ , but also the force constant, f, which is a measure of the bond strength. It is of interest to evaluate the influence of the heavier fluorine atom on the corresponding frequency in the ring molecule. The spring constant, f, can be related to the equilibrium bond length, r, by Badger's rule, (27)

242
$$f = a \cdot (r - d)^{-3}$$
. (3)

In Badger's original model, a is the Badger constant and d is the distance of the nearest approach of two nuclei in a biatomic molecule. For bonds between C and another element, a and d depend only on the period of the element in the periodic table. We use d = 0.61 for C-O single bond and C=O double bond in the current study. (28) For a polyatomic molecule, the electron cloud

surrounding two atoms under consideration would be overlapped by that of their neighbouring atoms. The complicated intramolecular coupling renders a varied "a" value for a satisfactory fit to experimental data.(28, 29) The equilibrium distance (r) between two atoms was obtained from the DFT calculation. The calculated spring constants and frequencies of the vibrational modes shown in Figure 3 are summarized in Table 1. From Table 1, the length of the C=O double bond is decreased by 0.011 Å from EC to FEC (see Figure 4 for the schematic of the related vibrations). The decreased bond length results in an increased spring constant for FEC and hence a slightly increased C=O stretching frequency (Table 1). Therefore, the FEC C=O stretching has a higher Raman shift than that of EC. Similar reasons can be drawn for the vibrations related to the ring structure. For example, the bond length of EC O3C4 (Figure 4) is 1.476 Å, whereas that of the FEC is 1.427 Å. This leads to an increased spring constant by 19.2%, assuming the same Badger constant value. Again, the ring breathing mode of FEC blueshift by 12 cm⁻¹ compared with that of EC at 717 cm⁻¹. Both the ring breathing mode and the ring deformation mode involve more than one vibrational mode and are fairly complicated. Thus, the agreement between calculated and experimental Raman shifts is remarkable. In order to apply the "ball and spring" model to the ring vibrations, the overall spring constant for the atom vibrations on the ring for the breathing mode (see supporting information) was evaluated. The overall spring constant of the ring is slightly larger for FEC than that for EC. Thus, the blueshift of some of the FEC vibrations versus their counterparts for EC should be attributed to the "stiffer" bonds upon the replacement of a hydrogen atom by a heavier fluorine atom in the methylene bridge. To demonstrate that nanogap SERS is a quantitative tool to study molecular fingerprints at the SLI of the aprotic solvents, we further performed SERS measurements on EC-DEC binary solvent with changing molar fraction of EC, X_{EC} . Complementary IR experiments were also carried out.

247

248

249

250

251

252

253

254

255

256

257

258

259

260

261

262

263

264

265

266

267

268

270 To make a clear comparison among spectra, all SERS spectra were normalized to the integrated DEC ρ_{CH3} band centered at 1122 cm⁻¹ and the IR spectra were normalized to the DEC ν_{sCH3} peak 271 centered at 1373 cm⁻¹. Figure 5 shows the SERS (top) and IR spectra (bottom) of EC-DEC 272 273 binary solvents with varied X_{EC} . While the intensity of many bands changes in both SERS and IR 274 spectra (Figure S1 shows full SERS and IR spectra of EC and DEC), we focused on the following three frequency regions due to their spectroscopic sensitivity to Li⁺ solvation: (30-32) 275 (I) EC ring breathing band (o_{O-C-O}) in 650-750 cm⁻¹, (II) EC ring deformation band (β_{C-C}), Figure 276 277 6. Example peak deconvolution of EC and DEC C=O stretching (in Region III) of (a) SERS and 278 (b) IR spectra for EC-DEC (0.5:1 vol) solvent. 279 DEC-CH₂ rocking band (ρ_{CH2}), EC skeletal stretching band (ν_{O-C-O}) and O-C-O bending band (δ_{O-C-O}) in 800-1000 cm⁻¹, and (III) carbonyl stretching band ($v_{C=O}$) for both EC and DEC in 280 281 1500-1900 cm⁻¹. For Region III, because the EC and DEC carbonyl bands are partially 282 overlapped, a peak deconvolution process is necessary for both SERS and IR spectra. Figure 6 283 shows the deconvoluted SERS (Figure 6(a)) and IR (Figure 6(b)) carbonyl bands for EC and 284 DEC (0.5:1: vol). The same process was applied to other EC-DEC mixtures. In Region I (Figure 5(a)), the SERS and IR spectra are much alike. Pure DEC (i.e. EC molar fraction $X_{EC} = 0$) shows 285 a small shoulder at 703 cm⁻¹, which could be assigned to OCOO bending band. (33) Even at the 286 lowest molar fraction of EC ($X_{EC} = 3.5\%$), the EC o_{O-C-O} at 717 cm⁻¹ (716 cm⁻¹ for IR) becomes 287 288 distinguished from others, and the peak intensity increases rapidly with increasing X_{EC} in the 289 EC-DEC binary solvents. 290 The integrated band absorbance (IR) and intensity (SERS) of the EC-DEC binary mixture is 291 plotted with respect to the molar concentration (C) of EC or DEC in Figure 7. Table 2 indexes 292 the EC molar fraction, X_{EC} to its molar concentration, C_{EC} for an ease of comparison between

Figure 5 and Figure 7. Figure 7(a) indicates that EC o_{O-C-O} peak integration ($A_{EC \circ O-C-O}$) quadratically depends on C_{EC} for both SERS and IR. The slope of the first order derivative of the quadratic fit for SERS is almost five times that of IR. This indicates that the SERS of EC o_{O-C-O} is more sensitive to C_{EC} than IR. For IR spectra in Region II (Figure 5(b)), it is noticeable that the band intensity of DEC ρ_{CH2} band (852 cm⁻¹) decreases with increasing X_{EC} , whereas EC ring stretching band (v_{O-C-O} , 970 cm⁻¹) increases in intensity. Only two weak peaks appear in the SERS spectra at these wavenumbers with no obvious trend with X_{EC} . At low EC concentration $(X_{EC} < 47.6\%)$, a single band is observed (902 cm⁻¹ for SERS and 901 cm⁻¹ for IR), which is assigned to DEC δ_{O-C-O} . Further increase of X_{EC} results in a blueshift of the SERS band to 897 cm⁻¹ and an IR satellite peak at 893 cm⁻¹. The blueshift is due to the increasing intensity of the EC ring skeletal deformation mode, β_{C-C} . The peak integration of EC β_{C-C} (897 cm⁻¹ for SERS and 893 cm⁻¹ for IR) band in Figure 7(b) indicates that a second order polynomial can describe the correlation between the integration of deconvoluted EC skeletal deformation band, A_{EC BC-C}, and EC molar concentration, C_{EC} , for both SERS and IR. Interestingly, in Figure 7(c), at the highest EC molar concentration (i.e. EC-DEC equivolume solvent), A_{DEC δO-C-O} is almost zero. A similar phenomenon occurs with the DEC carbonyl stretching band, $v_{C=0}$ at 1619 cm⁻¹ in Region III for SERS (Figure 5(c)). This may suggest that a higher dipole moment of the EC molecule in the nanogap results in surpassing SERS intensity over that of the DEC at high EC concentration. Thus, some bands of DEC nearly disappear in the SERS spectrum of the binary solvents above a critical value of C_{EC} . In Region III (Figure 5(c)), a prominent difference between the SERS and IR spectra is that the C=O stretching band for DEC $v_{C=O}$ is represented by a doublet for SERS (1735 cm⁻¹ and 1753 cm⁻¹). This is in sharp contrast to its IR counterpart, which exhibits a single fundamental mode at 1740 cm⁻¹ consistent with other studies. (30) It is worth noting that the

293

294

295

296

297

298

299

300

301

302

303

304

305

306

307

308

309

310

311

312

313

314

DEC $v_{C=0}$ shows only a single band at 1746 cm⁻¹ in conventional (non-SERS) Raman spectra. (6, 34) For SERS, the splitting of the DEC $v_{C=0}$ stems from Fermi resonance (FR), in which an overtone or a combination vibrational mode appears by gaining spectral weight from a fundamental mode. (35) More specifically, the vibration of linear DEC molecules entrapped in the interparticle nanogap is perturbed by the greatly enhanced EM-field and high field-gradient, leading to a distinct FR at a certain spectral frequency in this region. (35) The intensity of DEC $v_{C=O}$ increases with increasing C_{DEC} . The split of the EC carbonyl band (1785 cm⁻¹ and 1813 cm⁻¹ for SERS and 1773 cm⁻¹ and 1800 cm⁻¹ for IR) in this region is due to FR of the C=O stretching with the first overtone of the ring breathing. This doublet is less prominent for both IR and SERS when $C_{EC} < 5.0 \times 10^{-3}$ mol/mL. In an early study by Fortunato et al., (36) $v_{C=0}$ of neat EC at 313K exhibited a higher IR frequency (by 13 cm⁻¹) compared to that from Raman. The authors attributed this phenomenon as short-range orientation effects in dipolar aprotic liquids, which stemmed from a coupling between the transition dipoles of adjacent EC molecules. Interestingly, the EC $v_{C=O}$ in the EC-DEC equivolume mixture is 13 cm⁻¹ higher for SERS than that for IR. It might be due to a different intermolecular coupling of EC with surrounding DEC molecules in the nanogap. Clearly, the integrated intensity of the carbonyl modes of EC ($A_{EC, vC=0}$) and DEC $(A_{DEC \nu C=0})$ quadratically increase with C_{EC} and C_{DEC} , respectively for both IR and SERS (Figures 7(d) and (e)). Notably, there is an abrupt change of $A_{DEC, vC=0}$ at the low C_{EC} side (Figure 7(e)) for SERS, but not for IR. The discontinuity at $C_{EC} = 0$ might be attributed to the competitive adsorption of EC to the Au NP surface. A small amount of EC ($C_{EC} = 2.9 \times 10^{-4}$ mol/mL), may interrupt the FR of DEC $v_{C=O}$ within the nanogap, resulting in an abrupt decrease of $A_{DEC \nu C=O}$.

316

317

318

319

320

321

322

323

324

325

326

327

328

329

330

331

332

333

334

335

336

The reason that a quadratic correlation between the integrated Raman bands to the EC or DEC molar concentration in EC-DEC binary solvent can be explained as follows. The intensity of the Raman scattering is closely related to the polarizability of an individual molecule, α_I by (37)

$$341 I = C_i K l \alpha_1^2 \omega^4 (4)$$

where C_i is the mole concentration of species "i", K is composed of constants such as the speed of light. l is the laser power and ω is the incident radiation frequency. The microscopic polarizability of a molecule in the binary mixture is related to the macroscopic refractive index, n, of the dielectric media based on the Lorentz–Lorenz equation, (38)

$$346 \qquad \alpha_1 = \alpha_o \cdot \frac{n^2 - 1}{n^2 + 2} \tag{5}$$

347

348

349

350

351

352

354

355

356

where α_0 is a scalar which accounts for the polarizability of an individual molecule of species i in vacuum. This value is attenuated by the n-term, $(n^2-1)/(n^2+2)$, in Equation 5, leading to a changed polarizability in that dielectric, α_1 . This relation holds based on the agreement of the refractive indices of series EC-DEC mixtures calculated from the refractive index mixture rule and the experimental measurements (Figure 8(a)). The refractive index mixture rule is given by (39)

353
$$\frac{n^2 - 1}{n^2 + 2} = C_1 \frac{n_1^2 - 1}{n_1^2 + 2} + C_2 \frac{n_2^2 - 1}{n_2^2 + 2}$$
 (6)

which relates the refractive index of the binary mixture, n, to the refractive indices of individual species, n_1 and n_2 . Substituting Equation 5 to 4 yields a relation between Raman intensity and the refractive index of the EC-DEC binary solvent,

357
$$I = \alpha_o^2 \frac{9Kl\omega^4}{N_o^2} \cdot C_i \cdot \left(\frac{n^2 - 1}{n^2 + 2}\right)^2$$
 (7)

359

360

361

362

363

364

365

366

367

368

369

370

371

372

373

374

375

376

377

measured by a refractometer with 589 nm wavelength light, in the visible range like that of the Raman laser (785 nm) used for SERS study. The molar concentration of a species in an EC-DEC binary solvent is calculated by $C_i = X_i \cdot D/M$, where the molecular weight (M), density(D) and refractive index (n) of each EC-DEC mixture are listed in Table 2. The prefactor (denoted as "f") of Equation 7 is constant, independent of C_{EC} . The density of EC was taken from Reference, (40) whereas the rest EC-DEC mixtures were directly measured (Table 2). The plot of I/f versus the EC molar concentration, C_{EC} is shown in Figure 8(b). It can be seen that the quadratic fit surpasses the linear fit and better describes the relation between the SERS intensity and the C_{EC} . It should be noted that Lorentz-Lorenz assumes a constant local EM field implemented on a single molecule. This assumption needs to be further verified on the SERS of aprotic binary solvents with tuning the component molar ratio. It is also worth mentioning that a univariate analysis was often used to empirically fit the Raman scattering intensity (I) - species mole concentration (C_i) . However, in some cases, a linear relation fails to depict the I- C_i plot in a binary solvent system due to the absorption and/or resonance Raman effect, (41, 42) which was also observed in this study (Figure 8(b)). Higher-order empirical equations to describe the I- C_i relation are necessary in this sense. (26) Another contribution to the nonlinear dependence of the SERS intensity versus the mole concentration of species might stem from the intramolecular interaction in the Au NP gap region, which may lead to different preferred molecular orientations with respect to the local EM-field responding to the mole concentration of the components. The

The refractive index of a series EC-DEC solvents with varying EC molar refraction was directly

development of empirical equations between the SERS intensity with the component concentration in the EC-DEC binary solvent demonstrates that the nanogap SERS can be utilized as a semiquantitative tool to depict the liquid composition at SLI, which is critically important for an insightful understanding of the ion solvation/desolvation mechanism of SEI formation in the future.

While the analysis (Figure 5 to 7) on EC and DEC SERS and IR band integration dependence on EC mole fraction was based on selected peaks, more quantitative analysis on SERS and IR spectra with varying EC mole fraction in EC-DEC binary solvent was performed using principal component analysis (PCA) and multivariate curve resolution (MCR) analysis by a previously reported method. (4) The minimum number of spectral components needed in linear combination to obtain the sample spectra variation is determined by PCA. The pure component spectra were then extracted by MCR using alternating least-squares curve fitting. For both SERS and IR, two component spectra were found to be sufficient to describe the sample spectra variation with EC mole fraction, as shown in Figure 9(a). The component spectrum 1 is featured as DEC spectrum (i.e. $X_{EC} = 0$), whereas component spectrum 2 is dominated by EC spectrum. Both SERS and IR spectra show that the DEC component decreases with increasing X_{EC} , whereas spectra component of EC increases versus X_{EC} . It is interesting to notice that the threshold value was X_{EC} = 0.32, where SERS EC spectra starts dominating, smaller than that of the IR at X_{EC} close to 0.5. This confirms that at SLI, the EC molecule spectrum dominates even when DEC mole fraction is larger, in accordance with the analysis in Figure 5. This is intrinsically different than its bulk counterparts depicted by IR spectra.

399

378

379

380

381

382

383

384

385

386

387

388

389

390

391

392

393

394

395

396

397

400 Conclusions

We demonstrate that the nanogap mode SERS based on an Au NP monolayer is capable of probing and distinguishing the molecular vibrations of aprotic solvents with similar functional groups in close proximity to the solid/liquid interface. The SERS enhancement of those aprotic species increases by 3 to 5 orders of magnitude with respect to the standard Raman spectroscopy. The blueshift of carbonyl and ring-related Raman bands for FEC versus EC stems from the stiffer bonds between related atoms. The SERS band integration of selected peaks from either EC or DEC in EC-DEC binary solvent has a quadratic dependence on the EC or DEC molar concentration. The resultant empirical equations are useful to quantify the solvent concentration at the SLI region for future studies. This study unveils new avenue for a microscopic technique in vibrational spectroscopy of adsorbed species on the nanometer length scale from solid surface. The SERS technique in the current study should be readily applicable to areas where SLI is essential, such as water desalination, heterogeneous catalysis, electrophoresis, corrosion, mass transport across biomembranes, and batteries.

ASSOCIATED CONTENT

Supporting Information

- The following files are available free of charge.
- 417 SERS and IR spectra of EC-DEC binary mixtures, Raman peak assignment of DEC, EC and
- 418 FEC, overall ring spring constant evaluation for the EC/FEC ring molecule ring breathing mode
- 419 (PDF)

420 AUTHOR INFORMATION

Corresponding Author

422 Jagjit Nanda nandaj@ornl.gov 423 Guang Yang yangg@ornl.gov 424 Daniel T. Hallinan dhallinan@fsu.edu 425 **Author Contributions** 426 The manuscript was written through contributions of all authors. All authors have given approval 427 to the final version of the manuscript. 428 429 ACKNOWLEDGMENT 430 This research was conducted at Oak Ridge National Laboratory, managed by UT Battelle, LLC, 431 for the U.S. Department of Energy (DOE) under contract DE-AC05-00OR22725, was sponsored by the Office of Energy Efficiency and Renewable Energy (EERE) Vehicle Technologies Office 432 433 (VTO). SERS measurements were performed at the Center for Nanophase Materials Sciences, 434 which is a DOE Office of Science User Facility. GY thanks Dr. Ethan C. Self and Dr. Andrew 435 Westover for their fruitful discussion. RLS acknowledges support from the Fluid Interface 436 Reactions Structures and Transport (FIRST) Center, an Energy Frontier Research Center funded 437 by the U.S. Department of Energy, Officer of Science, Office of Basic Sciences. DTH 438 acknowledges funding from the 2017 LG Chem Battery Innovation Contest. 439 440 441 442

443 REFERENCES

- 444 1. K. Xu, Chem. Rev., 114, 11503 (2014).
- 445 2. K. Xu, A. von Cresce and U. Lee, *Langmuir*, **26**, 11538 (2010).
- 446 3. M. Gauthier, T. J. Carney, A. Grimaud, L. Giordano, N. Pour, H.-H. Chang, D. P. Fenning, S. F.
- 447 Lux, O. Paschos and C. Bauer, *J. Phys. Chem. Lett.*, **6**, 4653 (2015).
- 448 4. G. Yang, I. N. Ivanov, R. E. Ruther, R. L. Sacci, V. Subjakova, D. T. Hallinan and J. Nanda, ACS
- 449 Nano (2018).
- 450 5. I. Skarmoutsos, V. Ponnuchamy, V. Vetere and S. Mossa, *J. Phys. Chem. C*, **119**, 4502 (2015).
- 451 6. B. Klassen, R. Aroca, M. Nazri and G. Nazri, *J. Phys. Chem. B*, **102**, 4795 (1998).
- 452 7. M. Morita, Y. Asai, N. Yoshimoto and M. Ishikawa, J. Chem. Soc., Faraday Trans., 94, 3451
- 453 (1998).
- 454 8. K. Xu, J. Electrochem. Soc., **154**, A162 (2007).
- 455 9. M. Nie, D. P. Abraham, Y. Chen, A. Bose and B. L. Lucht, *J. Phys. Chem. C*, **117**, 13403 (2013).
- 456 10. E. Markevich, G. Salitra and D. Aurbach, ACS Energy Letters, 2, 1337 (2017).
- 457 11. A. Tornheim, M. He, C.-C. Su and Z. Zhang, J. Electrochem. Soc., 164, A6366 (2017).
- 458 12. I. A. Shkrob, J. F. Wishart and D. P. Abraham, *J. Phys. Chem. C*, **119**, 14954 (2015).
- 459 13. G. Yang, J. Nanda, B. Wang, G. Chen and D. T. Hallinan, ACS Appl. Mater. Interfaces, 9, 13457 460 (2017).
- 461 14. G. Yang and D. T. Hallinan, *Scientific Reports*, **6**, 35339 (2016).
- 462 15. M. W. Schmidt, K. K. Baldridge, J. A. Boatz, S. T. Elbert, M. S. Gordon, J. H. Jensen, S. Koseki,
- 463 N. Matsunaga, K. A. Nguyen and S. Su, *J. Comput. Chem.*, **14**, 1347 (1993).
- 464 16. A. D. Becke, *Phys. Rev. A*, **38**, 3098 (1988).
- 465 17. R. A. Kendall, T. H. Dunning Jr and R. J. Harrison, *The Journal of chemical physics*, **96**, 6796
- 466 (1992).
- 467 18. B. M. Bode and M. S. Gordon, *J. Mol. Graphics Modell.*, **16**, 133 (1998).
- 468 19. N. M. O'boyle, A. L. Tenderholt and K. M. Langner, J. Comput. Chem., 29, 839 (2008).
- 469 20. A. M. Michaels, M. Nirmal and L. Brus, *J. Am. Chem. Soc.*, **121**, 9932 (1999).
- 470 21. G. Yang, K. Kim, W. Wang, B. Chen, H. Mattoussi and D. T. Hallinan, *Macromol. Chem. Phys.*,
- 471 1700417 (2018).
- 472 22. H. Ko, S. Singamaneni and V. V. Tsukruk, *Small*, **4**, 1576 (2008).
- 473 23. G. Yang, L. Hu, T. D. Keiper, P. Xiong and D. T. Hallinan, *Langmuir*, **32**, 4022 (2016).
- 474 24. D. A. Genov, A. K. Sarychev, V. M. Shalaev and A. Wei, *Nano Lett.*, 4, 153 (2004).
- 475 25. M. Barbry, P. Koval, F. Marchesin, R. Esteban, A. Borisov, J. Aizpurua and D. Sánchez-Portal,
- 476 Nano Lett., 15, 3410 (2015).
- 477 26. I. R. Lewis and H. Edwards, Handbook of Raman spectroscopy: from the research laboratory to
- 478 the process line, CRC Press (2001).
- 479 27. R. M. Badger, *The Journal of Chemical Physics*, **2**, 128 (1934).
- 480 28. E. Kurita, H. Matsuura and K. Ohno, Spectrochim. Acta, Part A, **60**, 3013 (2004).
- 481 29. D. R. Herschbach and V. W. Laurie, *The Journal of Chemical Physics*, **35**, 458 (1961).
- 482 30. D. M. Seo, S. Reininger, M. Kutcher, K. Redmond, W. B. Euler and B. L. Lucht, J. Phys. Chem.
- 483 *C*, **119**, 14038 (2015).
- 484 31. M. Nie, D. P. Abraham, D. M. Seo, Y. Chen, A. Bose and B. L. Lucht, *J. Phys. Chem. C*, **117**,
- 485 25381 (2013).
- 486 32. J. L. Allen, O. Borodin, D. M. Seo and W. A. Henderson, *J. Power Sources*, **267**, 821 (2014).
- 487 33. J. Katon and M. Cohen, *Can. J. Chem.*, **53**, 1378 (1975).
- 488 34. M. G. Giorgini, K. Futamatagawa, H. Torii, M. Musso and S. Cerini, J. Phys. Chem. Lett., 6,
- 489 3296 (2015).
- 490 35. M. Sun, Y. Fang, Z. Zhang and H. Xu, *Physical Review E*, **87**, 020401 (2013).
- 491 36. G. Fini, P. Mirone and B. Fortunato, *Journal of the Chemical Society, Faraday Transactions 2*:
- 492 *Molecular and Chemical Physics*, **69**, 1243 (1973).

(2013).E. Talebian and M. Talebian, Optik-International Journal for Light and Electron Optics, 124, 38. 2324 (2013). W. Heller, The Journal of Physical Chemistry, 69, 1123 (1965). 39. D. Ward, R. Jones, J. Templeton, K. Reyes and M. Kane, ECS Transactions, 61, 181 (2014). 40. 41. C. Liu and R. W. Berg, Applied Spectroscopy Reviews, 48, 425 (2013). 42. M. Ludwig and S. A. Asher, Appl. Spectmsc., 42, 1458 (1988).

E. Smith and G. Dent, Modern Raman spectroscopy: a practical approach, John Wiley & Sons

37.

515 FIGURES

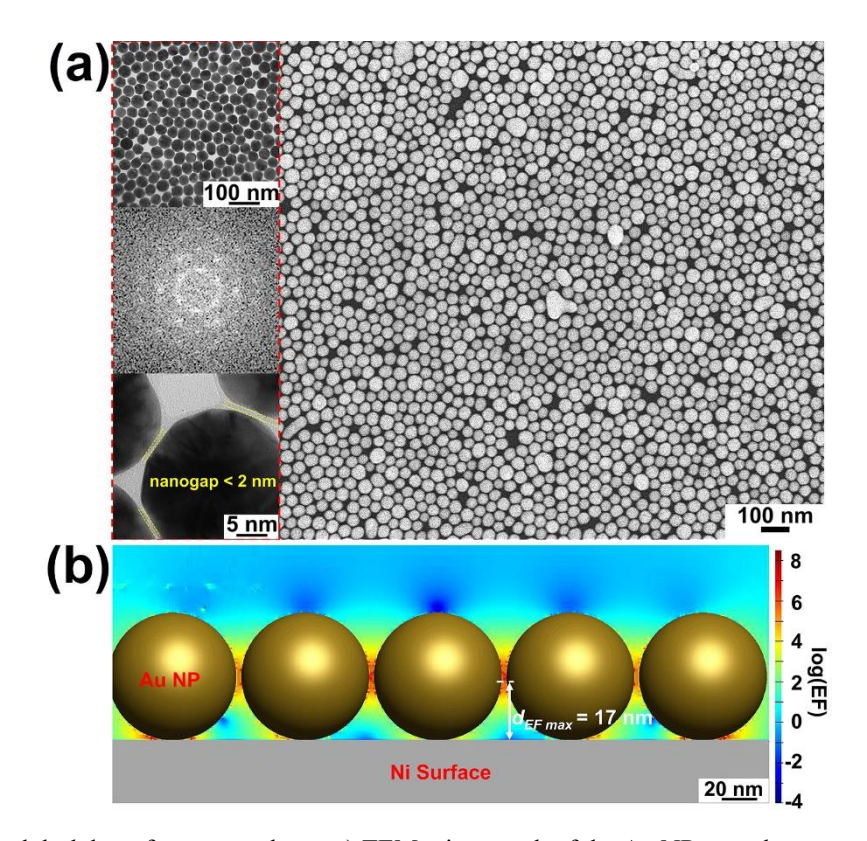


Figure 1. (a) (in red dash box, from top to bottom) TEM micrograph of the Au NP monolayer on copper grid, its fast Fourier Transform and a magnified TEM micrograph showing the nanogaps (marked by two parallel yellow dash lines) and SEM micrograph of Au NP monolayer on Ni-coated quartz substrate. (b) FDTD simulated enhancement factor (EF) distribution of the Au NP monolater on the Ni-coated quartz substrate. The maximum EF (\sim 8.2 x 10 8), in the nanogap region about 17 nm above the Ni surface, is denoted.

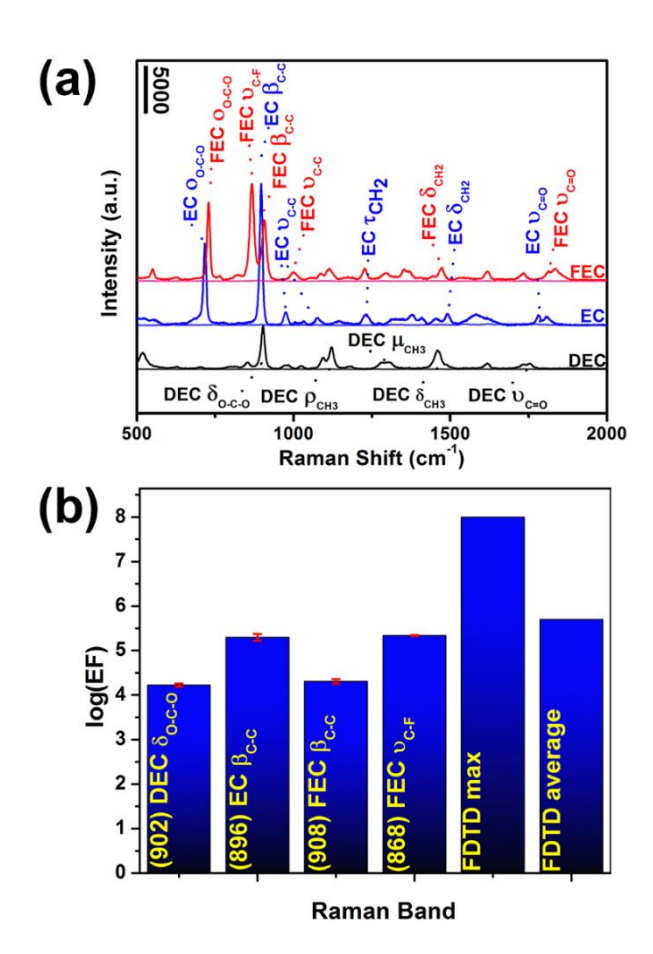


Figure 2. (a) SERS spectra taken from FEC, EC and DEC on Au NP film/Ni substrate, respectively. Standard Raman spectrum was taken for each corresponding sample on Ni as a reference, which is seemingly featureless in the same y-scale. The vibrational modes were marked by Greek symbols as follows, ν , stretching; δ , bending; ω , wagging; μ , deformation; τ , twisting; ρ , rocking; σ , ring breathing and σ , ring deformation. (b) The comparison of enhancement factor of various bands of different species and the FDTD calculated EF values. The error bar represents the standard deviation based on five measurements on random locations of the same species.

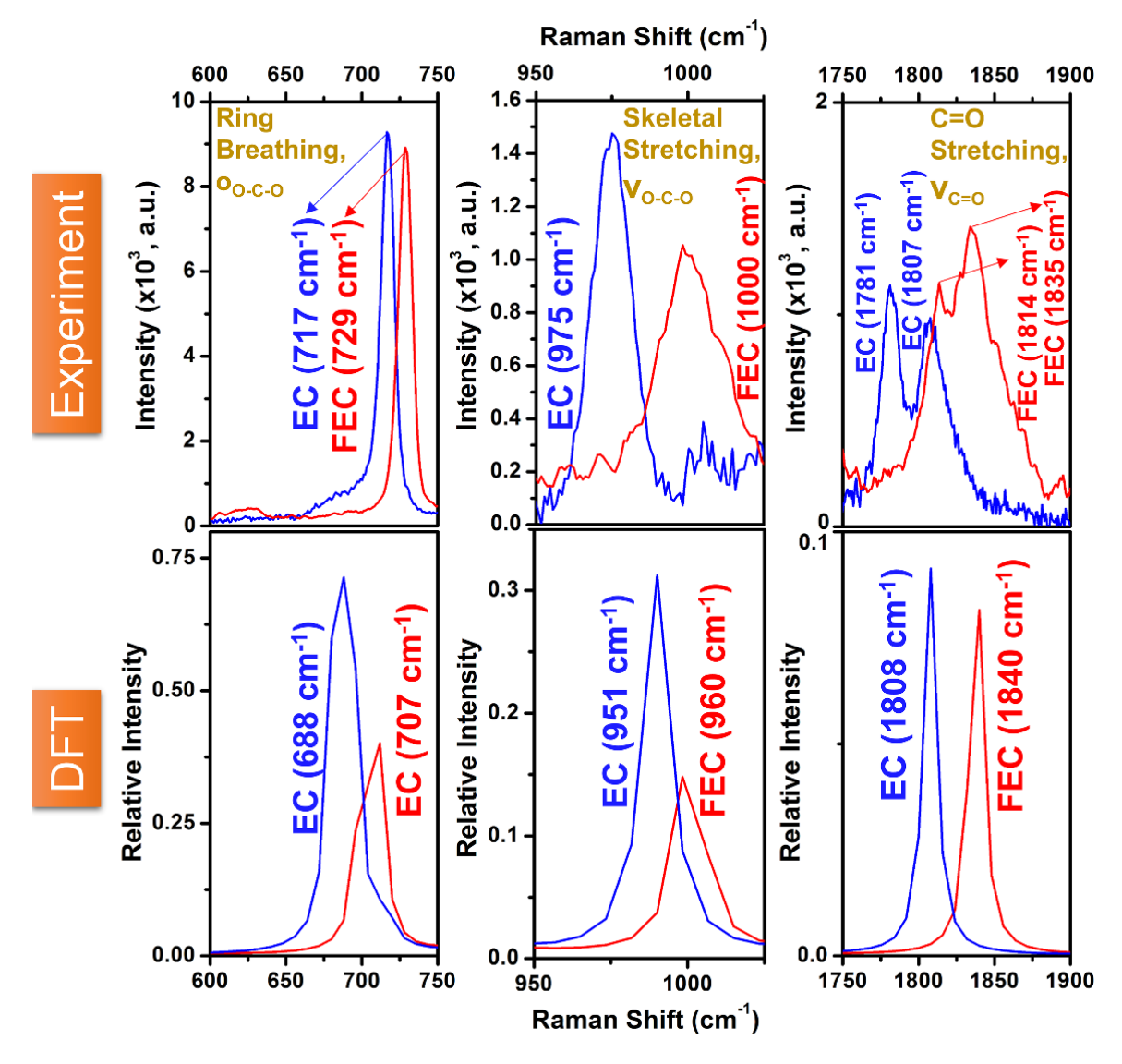


Figure 3. Comparison of the SERS spectra (top) between EC and FEC for three different Raman frequency regions. Lower panels show the DFT calculated Raman spectra of EC and FEC accordingly. Note that all spectra show only the calculated fundamental vibrations, and therefore do not include overtones or combination bands.

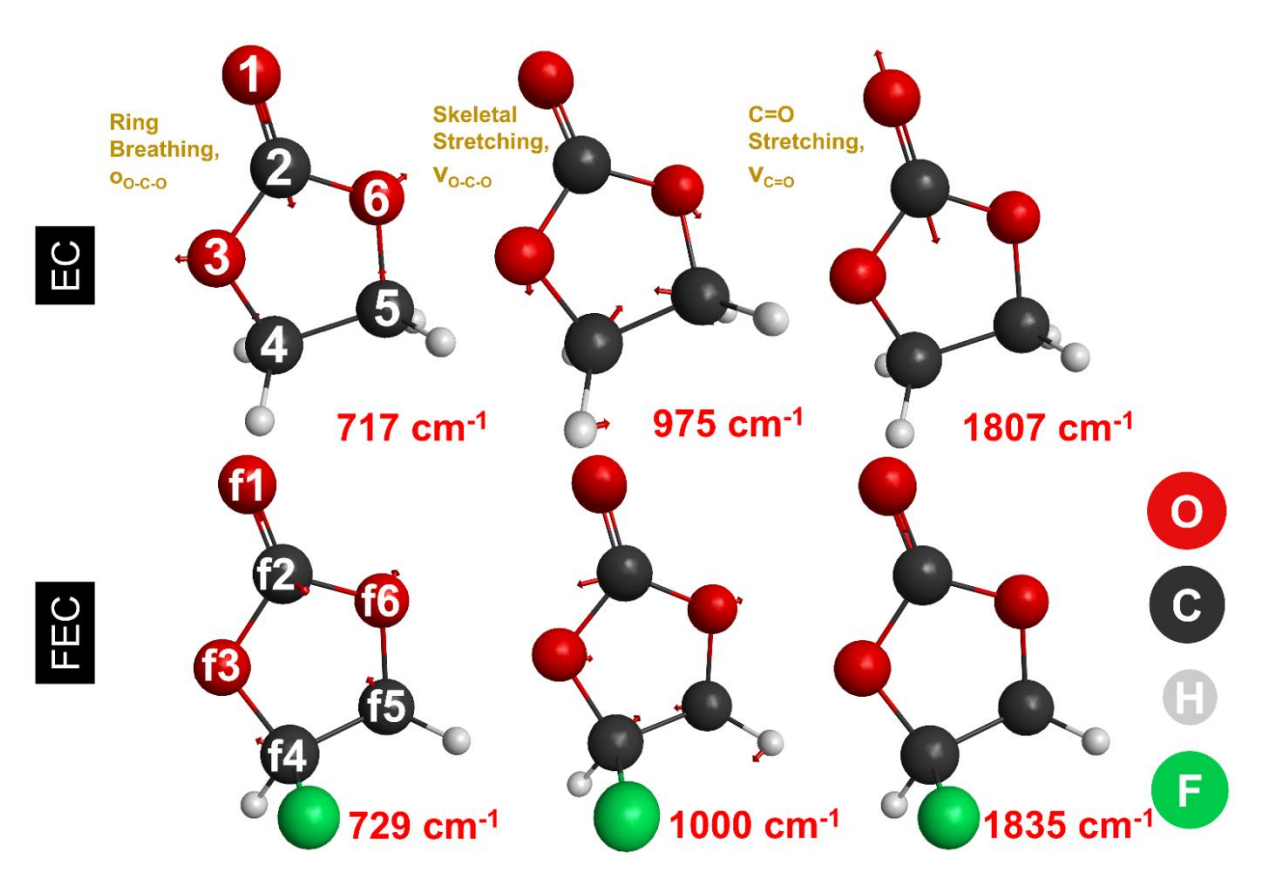


Figure 4. Schematic illustration of vibrational modes corresponding to each panel in Figure 3. (left) EC symmetric ring breathing and FEC out-of-plane ring breathing, (middle) EC in-plane ring deformation and FEC out-of-plane ring deformation, and (right) EC C=O stretching and FEC C=O stretching.

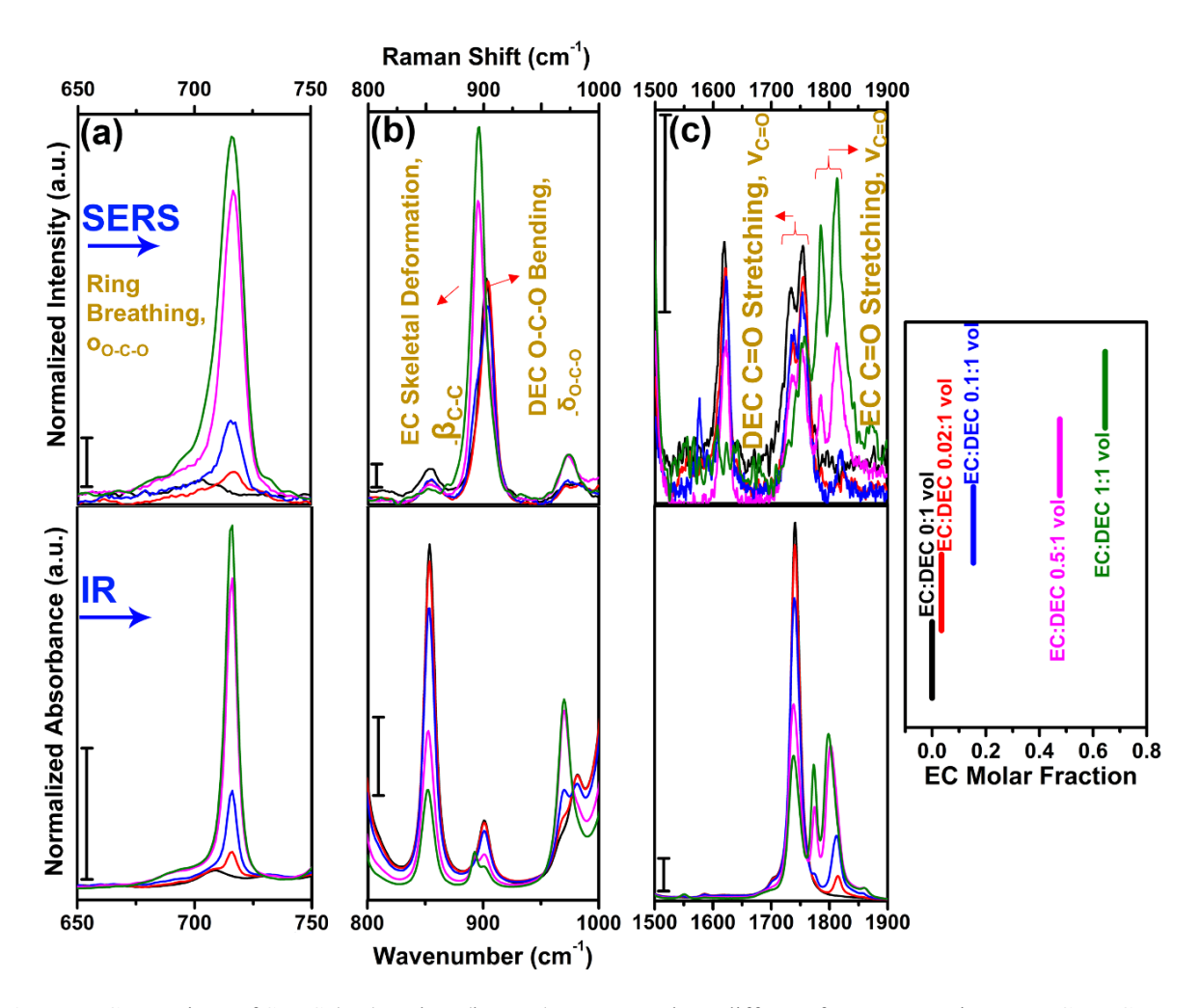


Figure 5. Comparison of SERS (top) and IR (bottom) spectra at three different frequency regions on EC-DEC binary solvents of different EC molar fractions, X_{EC} . The scale bar represents 0.2 for all plots and the legend on right relates the volume ratio of EC with DEC to X_{EC} . IR spectra are presented with ascending wavenumber for ease of comparison to SERS spectra.

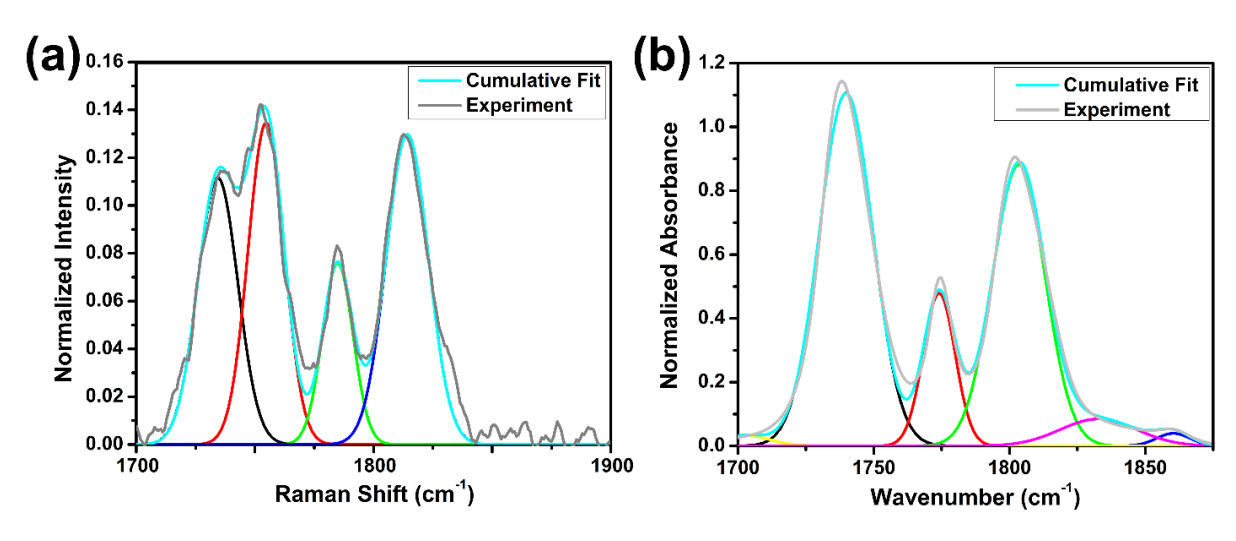


Figure 6. Example peak deconvolution of EC and DEC C=O stretching (in Region III) of (a) SERS and (b) IR spectra for EC-DEC (0.5:1 vol) solvent.

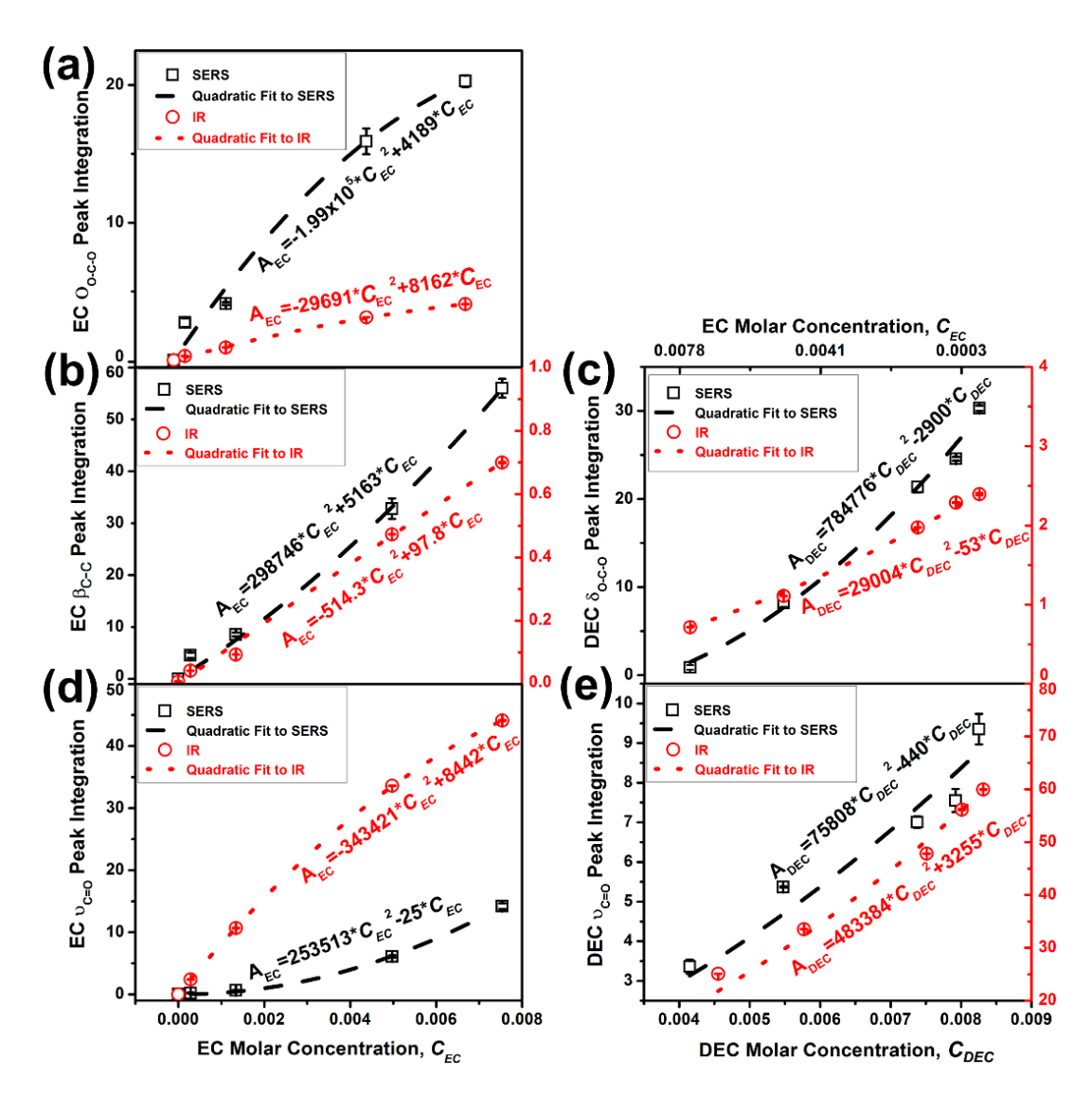


Figure 7. The plot and regression curves of the series of EC-DEC binary solvents for normalized SERS and IR band integration of the binary solvent versus the EC or DEC molar concentration (C). (a) EC o_{O-C-O} band integration at 717 cm⁻¹ versus C_{EC} . (b) Peak integration of EC β_{C-C} (896 cm⁻¹ for SERS and 893 cm⁻¹ for IR) band with respect to C_{EC} . (c) DEC δ_{C-O-C} (902 cm⁻¹ for SERS and 901 cm⁻¹ for IR) band integration with respect to C_{DEC} . (d) The plot of the band integration of EC vc=o versus C_{EC} and (e) the peak integration of DEC vc=o versus C_{DEC} . All regressions have passed the one-way F-test with a significance level of 0.01.

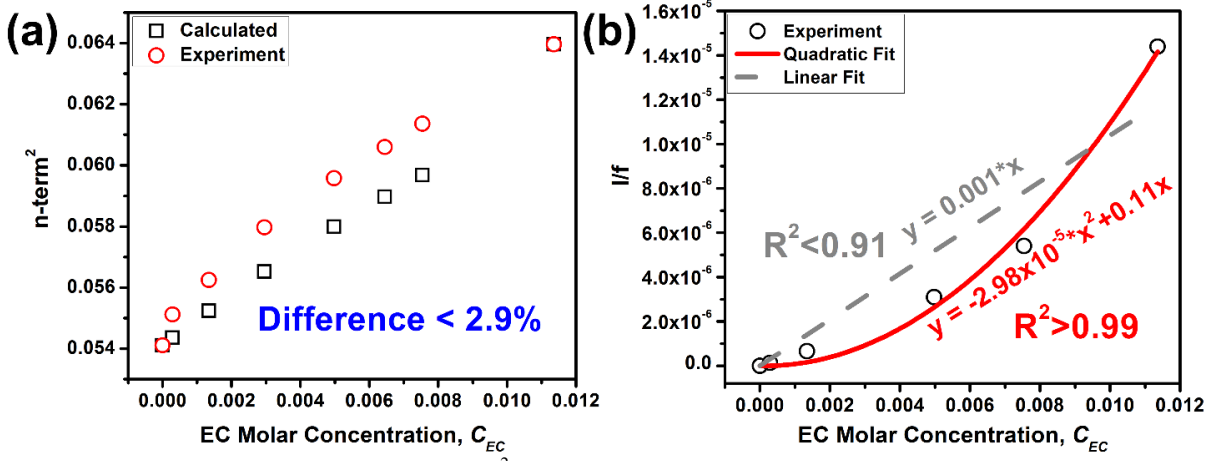


Figure 8. (a) Comparison between the n-term² from the calculated refractive index and that from the experimental measurement for each EC-DEC binary mixture. (b) Correlation between the ratio of the Raman intensity normalized by of the prefactor in Equation 7 (I/f) with respect to the EC molar concentration, C_{EC} .

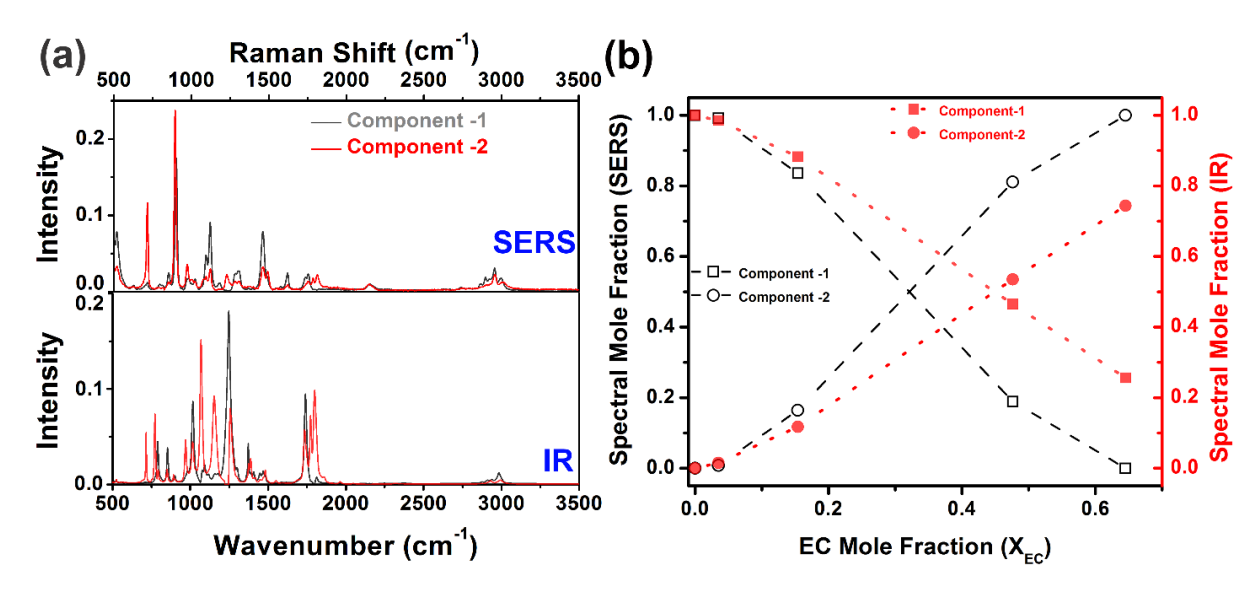


Figure 9. (a) The pure component spectra from PCA-MCR analysis for SERS and IR of EC-DEC binary solvent with varying EC mole concentration. (b) Mole fraction of two principal component spectra based on PCA-MCR analysis from SERS (left) and IR (right) spectra with changing molar fraction of EC-DEC binary solvent with different EC mole concentration.

594 TABLES

Table 1. Comparison of the atom bond length, spring constant and calculated Raman shift based on the ball and spring + Badger model for EC and FEC for related vibrations in Figure 3.

Vibration Mode	Contribution atoms*	Bond Length (Å)	Spring Constant (×10 ² N/m)	Calculated Raman Shift (cm ⁻¹)	Experimental Raman Shift (cm ⁻¹)
	EC C2-O6	1.395	2.07	715	717
Ring o _{o-c-o}	FEC Cf2-Of6	1.385	2.38	729	729
	EC C4-C5	1.542	3.46	1040	1030
Ring β_{C-C}	FEC Cf4-Cf5	1.527	3.63	1070	1077
	EC C2-O1	1.213	13.23	1810	1807
$\nu_{C=O}$	FEC Cf2-Of1	1.202	13.98	1860	1835

Table 2. The molecular weight, density and refractive index of all EC-DEC binary solvents.

EC molar fraction, X_{EC}	EC molar concentration, C_{EC}	Molar mass, M (g/mol)	Density, D (g/mL)	Refractive Index, n
0.04	2.9×10^{-4}	117.08	0.96	1.386
0.15	1.3×10^{-3}	113.51	0.99	1.396
0.31	3.0×10^{-3}	108.74	1.03	1.397
0.48	5.0×10^{-3}	103.81	1.08	1.403
0.58	6.5×10^{-3}	100.78	1.13	1.407
0.65	7.5×10^{-3}	98.73	1.15	1.410
1.00	1.1×10^{-2}	88.06	1.32*	1.420

^{*}According to reference 40, the volume change of EC right above melting point is less than 1%. Therefore, we do not expect a large deviation of the density of EC at 312 K from this value, at which SERS spectrum of EC was taken.